

The ISOPHOT - MAMBO survey of 3CR radio sources*: Further evidence for the unified schemes

M. Haas^{1,2}, S.A.H. Müller², F. Bertoldi³, R. Chini², S. Egner¹, W. Freudling⁴, U. Klaas¹,
O. Krause¹, D. Lemke¹, K. Meisenheimer¹, R. Siebenmorgen⁴, and I. van Bemmell⁵

¹ Max-Planck-Institut für Astronomie (MPIA), Königstuhl 17, D-69117 Heidelberg, Germany

² Astronomisches Institut, Ruhr-Universität Bochum (AIRUB), Universitätsstr. 150 / NA7, D-44780 Bochum, Germany

³ Max-Planck-Institut für Radioastronomie (MPIfR), Auf dem Hügel 69, D-53121 Bonn, Germany

⁴ European Southern Observatory (ESO), Karl-Schwarzschild-Str. 2, D-85748 Garching, Germany

⁵ Space Telescope Science Institute (STScI), 3700 San Martin Drive, Baltimore, MD 21218, USA

received 1. December 2003 ; accepted 3. June 2004

Abstract. We present the complete set of ISOPHOT observations of 3CR radio galaxies and quasars, which are contained in the ISO Data Archive, providing 75 mid- and far-infrared spectral energy distributions (SEDs) between 5 and 200 μm . For 28 sources they are supplemented with MAMBO 1.2 mm observations and for 15 sources with new submillimetre data from the SCUBA archive. The sample includes flat and steep spectrum quasars, broad and narrow line radio galaxies, as well as Fanaroff-Riley FR 1 and FR 2 types. The SED shapes exhibit a diversity in the infrared (IR), ranging from a smooth dominating synchrotron component in flat spectrum sources to a thermal dust bump around 60-100 μm in steep spectrum sources. The detection rate of a thermal bump in more than 50% of the cases suggests that dust emission may be a general phenomenon in these sources. We check the orientation-dependent unified scheme, in which the powerful FR 2 narrow line galaxies are quasars viewed at high inclination, so that their nuclei are hidden behind a dust torus intercepting the optical-ultraviolet AGN radiation and reemitting it in the infrared. We find that (1) both the quasars and the galaxies show a high mid- to far-infrared luminosity ratio typical for powerful AGNs and (2) – when matched in 178 MHz luminosity – both show the same ratio of isotropic far-infrared to isotropic 178 MHz lobe power. Therefore, from our large sample investigated here we find strong evidence for the orientation-dependent unification of the powerful FR 2 galaxies with the quasars. The distribution of the dust-to-lobe luminosity ratio shows a dispersion which we suggest to be most likely due to the additional influence of evolution and environment superposed on the orientation-dependent unification. We discuss our data also in the frame of the receding torus model. At the high 178 MHz luminosities of our sources above $10^{26.5}$ W/Hz we do not find any support for this model in its original formulation and therefore we propose a refinement: The scale height of the torus might not be independent of luminosity, rather it may increase at high luminosities due to the impact of supernovae from starbursts accompanying the AGN phenomena.

Key words. Galaxies: fundamental parameters – Galaxies: photometry – Quasars: general – Infrared: galaxies

1. Introduction

1.1. Unified schemes

While observationally at least a dozen classes of active galactic nuclei (AGN) are discernible, on the conceptional side consensus is growing that in most, if not all, of these different objects the accretion onto a massive black hole ($M_{\text{bh}} \geq 10^6 M_{\odot}$) provides the main source of energy. It seems natural to explain their apparent differences by observational effects such as (1) the *circumgalactic environment*, (2) the *evolutionary phase*, or

(3) the *aspect angle*. To disentangle these effects is one of the major challenges of the current AGN research, as reviewed by e.g. Urry & Padovani (1995).

The Revised Third Cambridge Catalogue of radio galaxies and quasars at 178 MHz by Laing et al. (1983, abbreviated 3CRR) and – applying softer criteria – by Spinrad et al. (1985, for short 3CR) contains 178 and 298 sources, respectively, which fall into several classes of radio-loud AGN:

- 1) flat spectrum quasars, which are almost core dominated,
- 2) steep spectrum broad line radio galaxies (BLRGs) and quasars (here collectively called *quasars*), with either compact or lobe dominated morphology,
- 3) powerful narrow line radio galaxies (NLRGs) of Fanaroff-Riley type FR 2 with – often asymmetric – jets ending in

Send offprint requests to: Martin Haas (haas@astro.rub.de)

* Based on observations with the Infrared Space Observatory ISO, an ESA project with instruments funded by ESA Member States (especially the PI countries: France, Germany, the Netherlands and the United Kingdom) and with the participation of ISAS and NASA.

- edge-brightened double lobes extending far beyond the host galaxy,
- 4) low power narrow line radio galaxies of Fanaroff-Riley type FR 1, with double jets feeding edge-darkened radio lobes often contained within the host galaxy.

The diversity and the brightness of the sources makes the 3CR catalogue a well suited database for studying the relationship between these AGN classes. The aspect angle relation between flat and steep spectrum quasars, with the flat spectrum sources being steep spectrum sources seen pole-on (as proposed by Orr & Browne 1982), is now widely accepted. The relation between steep spectrum quasars and FR 2 radio galaxies and that between FR 1 and FR 2 sources is still a matter of debate.

While the quasars show the optical signatures of a powerful AGN (like broad emission lines and high excitation and optical luminosity), the galaxies do not. In an early attempt, physically different central engines were proposed as reviewed by Begelman, Blandford & Rees (1984): quasars have a high mass accretion rate but a low black hole spin, and galaxies have a low mass accretion rate but a high black hole spin. Both engines should be able to create the radio jets. Although a viable explanation, from the conceptional view point it appears somewhat astonishing that two intrinsically different AGN types should lead to the *same* radio jet and lobe phenomena. Alternatively, in the picture of orientation-dependent unification, galaxies could be quasars in which the AGN is hidden behind a dust torus seen "edge-on", as proposed by Barthel (1989). Further debate arises from the fact that galaxies are distributed over the entire redshift range of the 3CR catalogue from the nearby local universe at $z \approx 0.01$ up to $z \approx 2$, but the quasars are preferentially found at larger distances at $z \gtrsim 0.3$ and 178 MHz luminosities above $10^{26.5}$ W/Hz (e.g. Singal 1996, Willott et al. 2000). The increase of the quasar fraction with distance and luminosity may find an explanation by the *receding torus model* (Lawrence 1991, Hill et al. 1996): due to dust sublimation the inner wall of the torus recedes with increasing luminosity of the central engine and – under the assumption that the torus scale height is independent of luminosity – the cone opening angle increases, leading to a higher chance to see the broad line region. However, it is still under debate how far this elegant model is valid for the powerful radio galaxies with 178 MHz luminosities *above* $10^{26.5}$ W/Hz. Alternatively, also physical or cosmic evolution could play a role: in this picture galaxies or a subset of them could be old quasars with a starving black hole, but still with luminous radio phenomena, possibly due to a favourable circumgalactic environment. Support for an environmental or evolutionary relationship comes from the fact that many FR 2s and most FR 1s fall into the low ionisation emission line category (Hine & Longair 1979), with little evidence for thick obscuring dust tori on HST images (Chiaberge et al. 1999, 2000).

In order to test the orientation-dependent unification between FR 2 galaxies and quasars, henceforth simply called *unification*, the task is to reveal a hidden powerful AGN in a (powerful) galaxy. Clear evidence for an AGN hidden behind a dust torus can be obtained by spectropolarimetry, when broad lines show up as light scattered in the bipolar cones with the polar-

isation angle being perpendicular to the polar axis (Antonucci & Miller 1985). Despite a number of cases with broad lines revealed by spectropolarimetry, in numerous cases huge extinction or dust lanes extended over kpc could have prevented the view into the central region via a "suitable mirror" (Antonucci & Barvainis 1990, Hill et al. 1996, Cohen et al. 1999). Note that the optical signatures of dust extinction only indicate that something *could* be hidden, but it remains to be shown that there is actually a powerful energy source behind the dust lanes. A robust check of the *unification* is to look for the mid- and far-infrared reemission of the absorbed light from the AGN. A great advantage is that at wavelengths $\lambda \gtrsim 25 \mu\text{m}$ the IR emission is largely optically thin, hence isotropic and independent of the aspect angle.

1.2. Infrared Observations

Observations of the 3CR sample with IRAS did not allow a substantial conclusion about the *unification* (Heckman et al. 1992, Heckman et al. 1994, Hes, Barthel & Hoekstra 1995, Hoekstra, Barthel & Hes 1997). The wavelength coverage and sensitivity of the IRAS observations were not sufficient to discriminate between dust and synchrotron emission in the individual sources, hence to correct for the contribution by a beamed synchrotron component to the mid- and far-infrared spectra of the sources.

With the Infrared Space Observatory ISO (Kessler et al. 1996) several small 3CR sub-samples were successfully observed: On the basis of a few ISOPHOT-MAMBO detections Haas et al. (1998) demonstrated that the IR emission of quasars and galaxies is a mixture of thermal and synchrotron radiation, dominated by thermal emission in radio-quiet quasars and synchrotron emission in flat spectrum radio-loud ones. Remarkably, steep spectrum quasars as well as galaxies showed powerful infrared dust emission.

In order to test the *unification*, a dedicated strategy compared galaxy – quasar pairs, which match in isotropic 178 MHz radio luminosity as well as redshift (in order to minimize possible cosmological effects). However, the four FR 2 galaxy – quasar pairs studied by van Bemmelen, Barthel & deGraauw (2000) yielded a lower detection rate of thermal dust emission and a lower dust luminosity for the galaxies than for the quasars, contrary to the expectations from the *unification*. On the other hand, ISOPHOT-MAMBO observations of ten FR 2 galaxy – quasar pairs with high radio power by Meisenheimer et al. (2001) yielded a balanced detection statistics and a similar dust luminosity for the quasars and galaxies, as predicted by the *unification*. Furthermore, the extrapolation of the synchrotron spectra of the quasars from the cm and mm regime into the far- and mid-IR has on average a more than ten times higher level than that for the radio galaxies. This is also consistent with the unified schemes, which predict that the jet axis of quasars is oriented more toward the line-of-sight, resulting in a stronger beamed component. Further ISOPHOT-MAMBO studies of small 3CR samples confirmed that many galaxies as well as quasars produce luminous dust emission (Andreani et al. 2002), and that the synchrotron component in quasars

is higher than in galaxies (van Bemmél & Bertoldi 2001). A closer quantitative look at the dust-to-radio luminosity ratio, however, reveals also differences between galaxies and quasars which suggest the additional role of evolution and environment superposed on the *unification* (Meisenheimer et al. 2001, Haas 2001).

Due to the limited detection of individual 3CR sources by IRAS, no definite conclusions about the *FR 1-FR 2 relation* could be drawn; to our knowledge neither ISO results on that topic have been reported so far.

1.3. This paper

In order to overcome the small number statistics and derive results from a broader statistical basis, we present here the remaining unpublished ISOPHOT SEDs of the 3CR sources in the ISO archive. We discuss the statistical properties of the complete mid- to far-infrared data base of 75 galaxies and quasars from the 3CR catalogue observed by ISOPHOT with regard to unification, evolution and environment as well as the applicability of the receding torus model. We focus here on the *unification*; the discussion of the *FR 1-FR 2 relation* will follow in a subsequent paper. Since common selection criteria for the sources were low cirrus foreground and good visibility to the satellite, this sample provides a fairly representative sub-sample of the 3CR catalogue, with a redshift range from nearby to distant ($z \lesssim 2$) objects. Throughout this paper we use blackbodies modified with a dust emissivity index of $\beta = 2$. We adopt a Λ cosmology with $H_0 = 71 \text{ km s}^{-1} \text{ Mpc}^{-1}$, $\Omega_{\text{matter}} = 0.27$ and $\Omega_{\Lambda} = 0.73$ (Bennett et al. 2003).

2. The data

The ISO Data Archive (Kessler et al. 2000) contains 5 to 200 μm photometry for 75 3CR sources obtained with ISOPHOT (Lemke et al. 1996), the photometer on board ISO. About half of them have also been observed between 5 and 15 μm with ISOCAM. Our sample does not contain those 3CR sources, for which only ISOCAM mid-infrared data are available, without any far-infrared complement by ISOPHOT data or IRAS detections. The full set of 85 ISOCAM observations is published by Siebenmorgen et al. (2004). Our sample does not include the two FR 1 sources 3C 71 (NGC 1068) and 3C 231 (M 82), which do not belong to the classical FR 1s with elliptical hosts, and which are nearby and therefore too extended to be observed in ISOPHOT photometry modes. In order to characterize the (sub)-mm part of the SEDs for the full sample, we complemented the available literature data: For 15 sources we found submm photometry in the JCMT-SCUBA archive, and performed additional mm observations for 28 sources with the Max-Planck Millimeter bolometer array MAMBO (Kreysa et al. 1998) at the IRAM 30 m telescope.

2.1. ISOPHOT

The observing modes (Laureijs et al. 2002) comprise chopped measurements, including those with the spectrome-

ter ISOPHOT-S, from which we determined broad band fluxes, and small maps.

We have reduced the data using the ISOPHOT Interactive Analysis tool (PIA¹ V10), together with the calibration data set V7.0. Using the latest versions of the data reduction tools, there are no systematic photometric offsets with regard to PIA V7 and V8 used for most of the results published earlier by various authors. The accuracy of the absolute photometric calibration depends mainly on systematic errors as described in Laureijs & Klaas (1999), and it is currently known to be better than 30% for faint sources. The relative filter-to-filter calibration agrees within 15% (Klaas et al. 2002).

2.2. MAMBO

With the MAMBO array at the IRAM 30-m telescope on Pico Veleta, Spain, during the pooled observation campaigns between January and March 2003, we obtained 1.2 mm (250 GHz) continuum flux densities for 28 of our sources. We used the standard on-off photometry observing mode, chopping between the target and sky at 2 Hz, and nodding the telescope every 10 s. The total on sky integration time varied between 2.5 and 23 minutes per source, and each object was observed at least twice, on different days. The absolute flux calibration was established by observations of Mars and Uranus, resulting in a flux calibration uncertainty of approx. 20%. The data were reduced using the MOPSI software package.

2.3. SCUBA

Yet unpublished submm continuum data obtained with SCUBA were retrieved from the JCMT archive for 15 sources. The observations were performed in photometry mode, and for one source (3C 274 = M 87) as jiggle maps. We have reduced them with the SCUBA User Reduction Facility (SURF), including identification of noisy bolometer pixels and removal of sky noise. The atmospheric transmission was determined from skydips and water radiometer data at the CSO. IRC+10206 and HL-Tau served as standard calibrators. The integration time per source was 10-20 min. In case of very good atmospheric transmission ($\tau_{\text{CSO}} \approx 0.05$) we also included the 450 μm data. The photometric accuracy at 450 μm and 850 μm is about 30% and 25%, respectively.

2.4. Literature data

ISO photometry of 49 3CR sources has so far been published by various authors, as labelled in col. “publ” of Table 1. The SED plots shown here include 4.5 to 14.3 μm data with ISOCAM (Cesarsky et al. 1996) for 33 sources, which are published by Siebenmorgen et al. (2004) and for a subset by Freudling et al. (2003).

Additional literature data were retrieved from the NED and SIMBAD, the 2MASS archive and numerous papers: Lilly &

¹ PIA is a joint development by the ESA Astrophysics Division and the ISOPHOT consortium led by the MPI für Astronomie, Heidelberg. Contributing institutes are DIAS, RAL, AIP, MPIK, and MPIA.

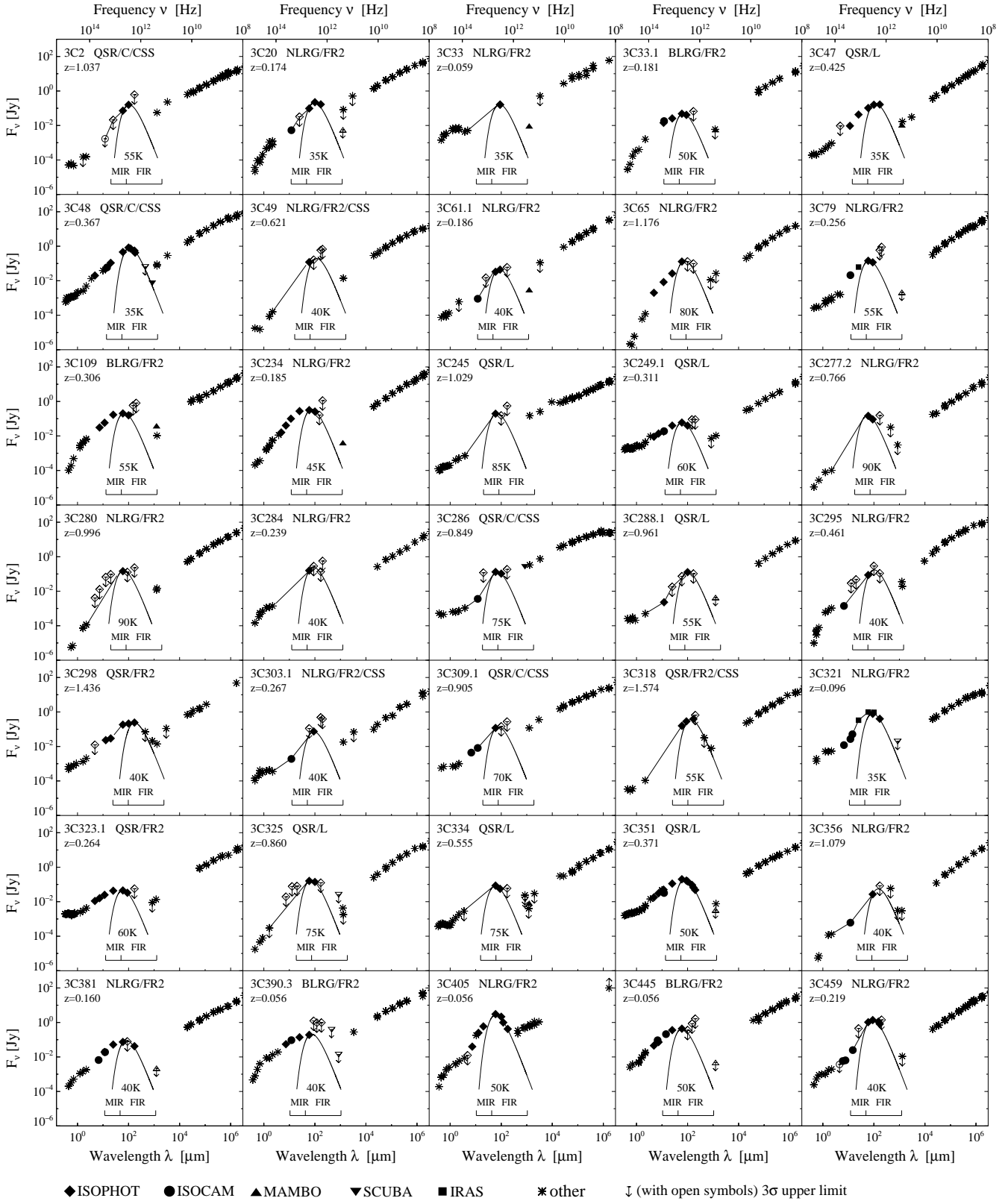


Fig. 1. Spectral energy distributions of those quasars, BLRGs and FR 2 NLRGs which show a clear thermal bump and are used in the discussion of the unification in Sect. 4.2. The measurement errors are of the size of the symbols. The wavelength and frequency ranges are as observed and not corrected to the rest frame of the objects. The MIR (10-40 μm) and FIR (40-1000 μm) wavelength ranges, as well as the temperature of the modified blackbody (solid line curve) fitted to the thermal FIR bump are shown in the object's restframe. Where the data coverage is sparse, the straight lines indicate the "envelopes" used for computing the restframe luminosities.

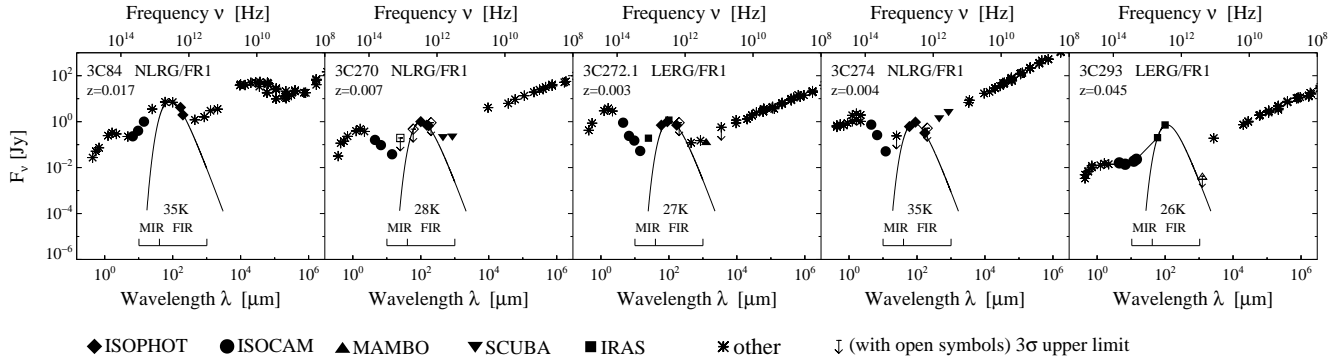


Fig. 2. Spectral energy distributions of the FR 1 sources. The meaning of the lines and labels is as in Fig. 1. Where the ISOPHOT data coverage is sparse, IRAS flux values from the NED are shown, if available (e.g. for 3C 293).

Longair (1984), Spinrad et al. (1985), Laing et al. (1983), Lilly et al. (1985), Neugebauer et al. (1987), Simpson et al. (2000) and de Vaucouleurs et al. (1991) at optical and NIR wavelengths, Chini et al. (1989a,b), Steppe et al. (1988, 1992, 1993), Robson et al. (1998), Hughes et al. (1993), Best et al. (1998), van Bemmelen et al. (2000), Polletta et al. (2000), Archibald et al. (2001), Willott et al. (2002), Andreani et al. (2002) and Stevens et al. (1998) at mm wavelengths, and at radio wavelengths from Jodrell-Bank Web pages (at <http://www.jb.man.ac.uk/atlas/>), Kühr et al. (1981), Kellermann et al. (1989) and Akujor et al. (1994).

3. Results

3.1. General properties

The IR, submm and mm fluxes of the 3CR sources are listed in Table 1. ISOPHOT achieved a detection rate of about 70% in the MIR ($\leq 25 \mu\text{m}$) and 60% in the FIR ($\geq 60 \mu\text{m}$). Even at the long wavelengths between 120 and $200 \mu\text{m}$ the detection rate is about 20%. The fluxes of the brightest non-variable sources, also detected by IRAS (e.g. 3C 272.1, 3C 405, 3C 459), agree within 15%.

14 out of 28 sources observed with MAMBO at 1.2 mm were detected, and $3\text{-}\sigma$ upper flux limits are provided for the others. From the 15 sources in the SCUBA archive eight were detected at $850 \mu\text{m}$ and three at $450 \mu\text{m}$.

Supplementing our data with further photometry from the literature as listed in section 2.4, we display the observed spectral energy distributions (SEDs) in Figs. 1, 2 and 3, whereby each Figure contains a subset of sources suitably chosen with regard to the illustration of the discussion items. Fig. 1 shows only those quasars, BLRGs and FR 2 NLRGs which exhibit a clear thermal bump and are used for investigating the *unification*. Fig. 2 shows the FR 1 SEDs. Finally, Fig. 3 shows the remaining SEDs which are either those of flat spectrum sources or which exhibit poorly constrained thermal bumps due to upper limits only – nevertheless illustrating the high IR luminosity limits. Note that the SEDs in Figs. 1 and 2 run smoothly and the photometric uncertainties represented by the size of the symbols are small.

The most remarkable feature of the SEDs in Fig. 1 is the steady increase in flux density from near- to far-IR wavelengths with a peak typically at $60\text{--}100 \mu\text{m}$, followed by a steep drop at (sub)-mm wavelengths in many cases. Where it could be measured, in particular for 3C 48, 3C 298, 3C 318, 3C 405, this drop follows exactly the Rayleigh-Jeans tail of the modified blackbody (with dust emissivity index $\beta = 2$). This strongly suggests a thermal nature of the FIR emission.

In order to discuss the SEDs in the framework of thermal emission, we have eyeball fitted a modified blackbody to the *peak* of the flux distribution, as shown in Figs. 1 and 2. The peak blackbody is mainly determined by the maximum in the FIR and, if available, also by the sub-millimetre points. However, this greybody fit does not always match the (sub)-millimetre measurements, since they may often be dominated by the synchrotron emission (for example in 3C 109 or 3C 234 in Fig. 1). Note that our “peak blackbody” corresponds in a νF_ν versus ν plot to the “break” of the thermal spectrum, where the slope equals unity. Its temperature T_p (corrected for redshift) lies between ~ 30 and 100 K , with higher T_p values preferentially found in the most luminous sources at high redshift – probably a natural consequence for a flux limited sample like ours. It is clear from Fig. 1 that also dust which is colder than the peak blackbody may be present, but if so, then at lower flux levels. Also, as being evident from the MIR data points above the peak blackbody curve, warmer dust components up to the dust sublimation temperature of about 1500 K are present, but for lucidity of the SED plots they are not shown explicitly here. Note that for the cases of upper limits and poorly determined dust bumps shown in Fig. 3 we tentatively adopt an average $T_p \sim 40 \text{ K}$ determined from the good cases shown in Fig. 1, if not constrained sufficiently.

The restframe thermal mid- ($10\text{--}40 \mu\text{m}$) and far-IR ($40\text{--}1000 \mu\text{m}$) luminosities are computed by integrating the SED “envelopes”. These curves are either sufficiently sampled by observations, as e.g. in the case of 3C 48, or they are partly sampled between 10 and $100 \mu\text{m}$ and follow the Rayleigh-Jeans tail of the peak blackbody between 100 and $1000 \mu\text{m}$, as e.g. in the case of 3C 47. For a few sources in Fig. 1 (3C 33, 3C 49, 3C 245 and 3C 284) the SEDs are sparsely sampled in the MIR-FIR regime; in these cases they are interpolated linearly in the log-

log SED plots between NIR and FIR flux points as indicated by the solid lines. Since the short wavelength part of the integration interval dominates the luminosity calculation, for poorly sampled SEDs the MIR luminosity may be overestimated by up to $\sim 50\%$, but the FIR luminosity is not significantly ($< 15\%$) affected by the choice of T_p .

For all sources Table 2 lists the derived parameters like luminosities, dust temperatures and masses, and other values used in the discussion.

3.2. Notes on some individual sources

3C 274 (M 87): The SED of this FR 1 source clearly exhibits as three basic features (1) the optical-NIR bump from the host galaxy, (2) the thermal dust bump in the mid- and far-IR, and (3) the radio synchrotron component. Table 1 lists the total fluxes at 450 and 850 μm , nevertheless we were able to resolve the one-sided jet and the core in the SCUBA jiggle maps. The core fluxes assuming a point source with FWHM $8''$ and $15''$ are 0.391 ± 0.10 Jy and 1.085 ± 0.10 Jy at 450 and 850 μm , respectively.

3C 268.4: Our FIR fluxes at 90 and 170 μm are similar to those reported by Andreani et al. (2002), but they are surprisingly high for a quasar at $z \approx 1.4$. Therefore we checked for the presence of other nearby galaxies. In fact, the galaxy NGC 4138 lies less than $200''$ apart and has an extent of more than $100''$. In the FIR it is also bright with $F(170 \mu\text{m}) > 6$ Jy, as we found with the help of the ISOPHOT Serendipity Survey (Stickel et al. 2000). Hence the large ISOPHOT beams of $45''$ and $180''$, respectively, have seen mainly the contamination by NGC 4138. Therefore, we do not consider 3C 268.4 any further.

3C 313: The FIR flux reported by Andreani et al. (2002) is due to a misidentification, actually the ISO observations refer to IRAS F15086+0801 (\neq 3C 313).

3C 368: The source was observed three times in the MIR 5–15 μm range, once with ISOPHOT on Oct. 18, 1996 (at 4.8 and 7.3 μm) and twice at 12 μm with ISOCAM on Feb. 27, 1996, and on Oct. 27, 1997. The detections on Oct. 18, 1996 exceed by far the 3σ upper limits from Feb. 27, 1996 and Oct. 27, 1997. The ISOPHOT chopped series show a perfectly oscillating on-off pattern leaving no doubt about the reality of the source detection. Since the explanation of strong MIR variability of 3C 368 seems unlikely to us, we suggest that the “MIR flux excess” during the observations on Oct. 18, 1996 is due to the passage of an asteroid (or comet), seen in the ISOPHOT aperture. However, no so far known asteroid has crossed the ISOPHOT observations (private communication by Thomas Müller). Nevertheless, an asteroid (or comet) seems to be the best explanation for the spurious 3C 368 detection and non-detections. Furthermore, at a temperature of 230 K as indicated by the MIR fluxes, an asteroid superposed on the 3C 368 field of view does not affect the FIR fluxes of 3C 368 at $\lambda \geq 60 \mu\text{m}$. Since 3C 368 was also detected with SCUBA at 450 μm (Archibald et al. 2001), we ascribe the FIR-submm dust bump to 3C 368 and use the ISOCAM upper limit for MIR luminosity estimates. Nevertheless, we do not include 3C 368 in the discussion here.

3C 390.3: This broad line radio galaxy was also detected by IRAS, but both the ISOPHOT and the ISOCAM MIR data do not confirm the exceptionally high 12 and 25 μm IRAS fluxes (Miley et al. 1984), thus making the mid- to far-IR colours of 3C 390.3 more similar to those of other BLRGs. The high IRAS fluxes could be contaminated by an asteroid or comet.

3C 454.3: This is one of the few examples of a *flat* spectrum quasar with a strong FIR dust bump sticking out of the bright synchrotron continuum. Other such examples are 3C 273 (Fig. 3), 3C 279 (Haas et al. 1998) and PG 1302-102 (Haas et al. 2000). We checked, whether the bump in 3C 454.3 could be due to another galaxy, but the only candidate on DSS and 2MASS images is an unresolved object about $15''$ NNE with a K-star like optical-NIR SED. Therefore we conclude that the bright FIR dust bump is in fact caused by 3C 454.3.

4. Discussion

Figs. 1 and 2 demonstrate that at least half ($> 40/75$) of the 3CR SEDs display a mid- to far-infrared bump due to thermal emission by dust. Even in the remaining cases the upper limits allow for considerable dust emission (Fig. 3, Table 2). In the following we consider the different classes (e.g. flat and steep spectrum quasars, BLRGs, FR 2 NLRGs and FR 1s), and investigate how the dust emission compares to the properties at other wavelengths. First, we discuss the SED shapes for representative class members. Then we study the statistical properties of the FR 2 NLRGs, quasars and BLRGs with respect to the *unification*, whereby we also consider other effects like those predicted by the receding torus model as well as evolution and environment.

4.1. SED shapes

The SEDs shown in Figs. 1 and 2 exhibit a striking diversity of shapes. Figure 4 shows five representative examples among the different AGN classes, i.e. radio and optical types:

1) Flat spectrum core dominated quasars (“FSQs”) like 3C 454.3: The synchrotron spectrum extends at a nearly constant flux level from the cm to the mm range, and declines at shorter wavelengths. In the FIR, the SEDs may show a thermal dust bump, as in the powerful FSQ 3C 454.3, or not, as in the less luminous BL Lac object 3C 371 (Fig. 3). In the context of unified schemes these flat spectrum sources are viewed nearly pole-on as proposed by Orr & Browne (1982).

2) Steep spectrum quasars like 3C 351: The synchrotron spectrum drops from the cm to the mm wavelengths, so that the thermal FIR dust emission bump becomes clearly visible. The optical spectra are quite blue, typical for an AGN outshining the host galaxy. Also, the SEDs show a power-law like flux increase, from the NIR over the MIR and peaking in the FIR, as seen also in optically identified PG quasars (Haas et al. 2003). With respect to the optical flux, the FIR dust bump may be quite pronounced with a steep slope from the NIR to the FIR as in 3C 48 at $z \sim 0.3$ and 3C 318 at $z \sim 1.5$ or more shallow as in 3C 249.1 at $z \sim 0.3$ and 3C 298 at $z \sim 1.5$ (Fig. 1). We do not see any difference between the SEDs of FR 2, lobe dominated and CSS types.

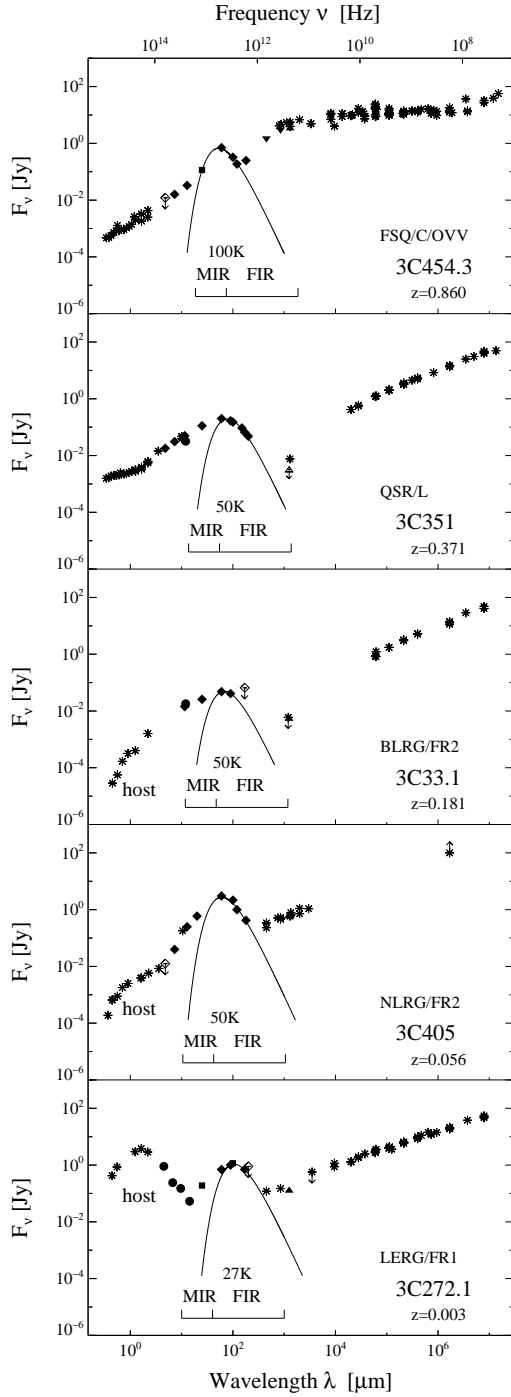


Fig. 4. SED shapes of 3CR sources as representative examples of the different optical and radio classes, having good spectral data coverage. The symbols are as in Fig. 1.

3) Broad line radio galaxies (BLRG) like 3C 33.1: The *infrared* and *radio* spectra are similar to those of the quasars, showing in the IR also the powerlaw rise between 5 and 60 μm . In contrast, the *optical* spectrum is redder than that of quasars, probably due to a stronger contribution of the host galaxy relative to that of the AGN, and possible obscuration of the intrinsically blue central spectrum.

4) Narrow line radio galaxies (NLRG) of class FR 2 like 3C 405: The far-infrared and radio spectra are similar to those of quasars and BLRGs. Relative to the FIR, however, the emission in the optical and also in the NIR is weaker. This suppression at short wavelengths shows some range: while for 3C 405 the optical-NIR SEDs are only “moderately” reddened, the optical to IR slope is very steep for both 3C 65 and 3C 234 (Fig. 1). In the unified scheme the NLRGs of class FR 2 represent edge-on quasars. 3C 234 shows polarised broad H_α but narrow H_β lines (Antonucci 1984); hence it might be seen at the grazing angle to the edge of the dust torus. Some NLRGs of class FR 2 like 3C 321 and 3C 459 (Fig. 1) show a strong FIR bump and only a moderate MIR contribution, more reminiscent of the SEDs of starburst galaxies.

5) Narrow line and low-excitation radio galaxies (LERG) of class FR 1 like 3C 272.1, showing three basic SED features:

- 1) in the optical-NIR a bright bump due to the elliptical hosts, represented by a blackbody of $T \approx 3500$ K peaking at about $1 \mu\text{m}$,
- 2) in the cm-mm wavelength range a steep synchrotron spectrum, and
- 3) in the MIR-FIR a well discernible dust emission bump.

The examples shown in Fig. 4 illustrate the basic SED features. In the optical they arise from the host galaxy and the blue AGN continuum, in some cases reddened by extinction toward the central region. In the IR and radio ranges the emission from dust and from the jet and lobes can well be discerned. Remarkably, the SEDs exhibit also a diversity of shapes even within each AGN class, for example in the strength of the FIR dust bump or the slope between the NIR and FIR fluxes. For the optically selected PG quasars, which are thought to be seen nearly pole-on, such differences in the IR emission could be interpreted as evolution of the dust distribution around the heating sources (Haas et al. 2003). Although the diversity of SED shapes within each 3CR AGN class may also indicate such intrinsic differences, the orientation with respect to the line of sight is not yet known for our 3CR sample and it is still under debate, how far the observed near- and mid-IR emission is influenced by different viewing angles. Therefore, we will restrict our investigation to the orientation problem. Furthermore, average SEDs for each AGN class could be computed, but they will smear out the details recognisable in the individual SEDs. Therefore, instead of using averages, in the next subsection we prefer to analyse the properties from the individual SEDs.

4.2. On the FR2 unification

In this section we consider the following two basic classes: i) the steep spectrum quasars and the BLRGs, henceforth for short denoted as *quasars*, and ii) the FR 2 NLRGs, henceforth denoted as *galaxies*. The strategy to check the *unification* includes two steps: (1) to show that both the *quasars* and the *galaxies* exhibit a high mid- to far-IR luminosity ratio typical for AGNs, and (2) that the isotropic FIR-to-radio luminosity ratio is the same for *quasars* and *galaxies* at matched isotropic 178 MHz radio power. We consider only those sources shown

in Fig. 1, which have sufficiently well sampled SEDs. The sample investigated here consists of 17 *galaxies* and 18 *quasars*, hence it can be considered as balanced. The set of sources shown in Fig. 3 and not included here comprises 20 *galaxies* and 15 - partly flat spectrum - *quasars*, and we will see below that their exclusion does not introduce a strong bias.

4.2.1. AGN typical dust emission

The thermal 10-1000 μm infrared luminosities of our sample span four orders of magnitude, from moderate $10^{10} L_{\odot}$ over luminous $10^{11} L_{\odot}$ and ultraluminous $10^{12} L_{\odot}$ to hyperluminous 10^{13} - $10^{14} L_{\odot}$ objects (Table 2 and abscissa of Fig. 5). The most luminous objects lie at the highest redshift, as is typical for flux limited samples like the 3CR catalogue.

The dust masses derived from the peak blackbodies shown in Fig. 1 range between 10^6 and $10^9 M_{\odot}$ (Table 2), which is comparable to those found in PG quasars (Haas et al. 2003) and in ULIRGs (Klaas et al. 2001). Although the derived dust masses are possibly uncertain by a factor of ten, they do still provide a rough estimate of interstellar material associated with these objects.

In order to compare the 3CR sources with other samples of known properties, we have decomposed the IR emission into the MIR (10-40 μm) and FIR (40-1000 μm) luminosities (Table 2). For the *quasars* as well as for the *galaxies* the mid-to far-infrared luminosity ratio ranges between 0.4 and 5 as shown in Fig. 5. This is comparable to what is found for optically selected PG quasars (Haas et al. 2003). In contrast, those ultraluminous infrared galaxies (ULIRGs), in which the dust emission is powered mainly by starbursts and *not* by an AGN, populate the $L_{\text{MIR}}/L_{\text{FIR}}$ range from 0.15 to 0.5 (Klaas et al. 2001). This is significantly lower than that of both the *quasars* and the *galaxies*. Therefore, the high mid- to far-infrared luminosity ratio above 0.5 together with the high dust luminosity ($L_{\text{IR}} \gtrsim 10^{11} L_{\odot}$) provides evidence for the presence of a powerful AGN in the *quasars* and the *galaxies* as well. Their AGN may be accompanied by starbursts, but for our purpose here the presence of a powerful buried AGN in the *galaxies* is relevant. It argues in favour of the *unification*. It should be noted here, that the orientation-dependent unification picture may not apply for the FR 1 and the low-power FR 2 sources, which have relatively low dust luminosities and masses.

A closer look on the mid-to-far-infrared luminosity ratio shows that the *quasars* lie above unity, while many of the *galaxies* lie below unity (Fig. 5). Such a difference between *quasars* and *galaxies* is consistent with unified models, if the proposed dust torus becomes optically thick at MIR wavelengths (Pier & Krolik 1992, 1993, van Bemmél & Dullemond 2003). In this case, if seen edge-on, our view towards the hot MIR emitting dust at the inner walls of the torus will suffer from extinction even at MIR wavelengths by the outer parts of the torus or by more extended dust. The actual degree of MIR opacity is not yet known. A value of $A_{\text{MIR}} \sim 1$ -2 is needed to explain the lower $L_{\text{MIR}}/L_{\text{FIR}}$ ratios for the *galaxies*. Using standard extinction curves this value corresponds to $A_V \sim 100$ -200, hence not exceptional with regard to that found in ULIRGs

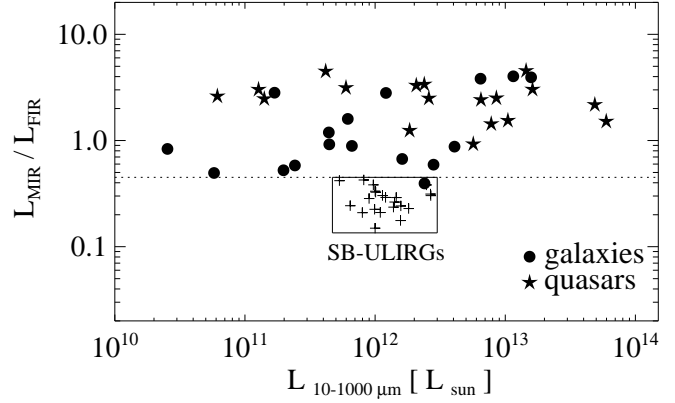


Fig. 5. Mid- to far-infrared dust luminosity ratio versus 10-1000 μm luminosity. The rectangular box shows the range of local starburst ULIRGs (from Klaas et al. 2001), each plotted with a "+" sign, and the dotted line indicates the upper end of their $L_{\text{MIR}} / L_{\text{FIR}}$ distribution. The only 3CR source falling below this line is 3C 459.

(e.g. Haas et al. 2001). Therefore we do not yet see any conflict with the *unification* and further investigations with more detailed observations as well as models may clarify that issue.

4.2.2. Radio-Infrared-Comparison

So far we have found evidence for a powerful AGN in both the *quasars* and the *galaxies*. In a strict sense, however, the concept of *unification* requires that for an object drawn from the parent population any isotropic emission remains the same while rotating the viewing angle to its axis. Thus, for an ideal sample of parent objects the emitted isotropic FIR dust power should be the same for objects of identical isotropic lobe power. Therefore, following the ideas by Meisenheimer et al. (2001), we consider R_{dr} , the ratio of P_{ν} at FIR wavelength 70 μm ($= 4.3 \text{ THz}$) and P_{ν} at radio frequency 178 MHz. Figure 6 shows R_{dr} versus the 178 MHz radio lobe power. All along the range of the 178 MHz radio lobe power, the distribution of R_{dr} for the *quasars* is strikingly similar to that of the *galaxies*. There is a marginal impression of a decline of R_{dr} with 178 MHz radio lobe power. This trend, however, is most likely caused by the mathematical dependency " a/x versus x ". It disappears when plotting R_{dr} versus L_{IR} (Fig. 6 bottom). As a quantitative check, we divide the luminosity range into two bins, one for luminosity below $2 \cdot 10^{12} L_{\odot}$ and one above, and calculate for each bin the mean R_{dr} values. They lie in the range of $10^{2.0 \pm 0.3}$ (Table 3). Again, a possible marginal decline of the mean R_{dr} with increasing luminosity is not yet statistically significant and we discuss possible reasons further below (Sect. 4.2.3).

With regard to the "matching strategy" applied by van Bemmél et al. (2000) and Meisenheimer et al. (2001) this means that, if we choose a *galaxy* - *quasar* pair matching in 178 MHz radio lobe power, i.e. lying in a vertical bin of Fig. 6, they exhibit a similar R_{dr} , exactly as predicted by the unified schemes. Some exceptional cases are discussed below. Also, if

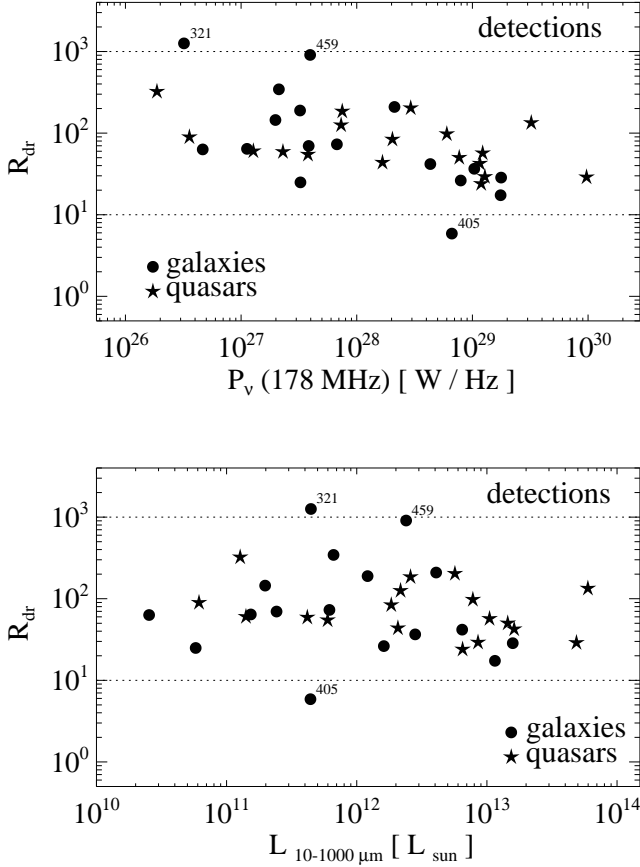


Fig. 6. *Top:* Ratio of far-infrared dust power to radio lobe power R_{dr} versus radio lobe power, at restframes $70 \mu m$ and $178 MHz$. *Bottom:* R_{dr} versus L_{IR} . The dotted lines indicate the range of the dispersion discussed in the text, and the extreme sources 3C 321, 3C 405 and 3C 459 are labelled explicitly.

we plot R_{dr} versus redshift, or if we use the MIR power at $15 \mu m$ (with values given in Table 2) instead of the FIR power at $70 \mu m$, all along the abscissa the R_{dr} distributions look quite similar for *galaxies* and *quasars*.

As illustrated in Fig. 7 with values given in Table 3, the FR 2 NLRGs and quasars from Fig. 3, for which we obtained only upper limits for the dust luminosity, populate the same range of R_{dr} as the detected sources from Fig. 1 do. Obviously the upper limits are so high that their constraints are consistent with our conclusions on the *unification*. Future data with the Spitzer and HERSCHEL satellites may consolidate this.

The range of R_{dr} values spans a factor of about ten around the average $R_{dr} \sim 100$ as indicated by the dotted lines in Fig. 6. This appears large at first glance, but it becomes actually small with regard to the range of more than four decades of power. In view of the complexity of the objects, with a diversity of the strength of the thermal IR dust bump, evolving giant radio lobes (Kaiser et al. 1997, Blundell & Rawlings 1999) and various circumgalactic environments (Barthel & Miley 1988), such a dispersion is certainly not surprising. Therefore, the strik-

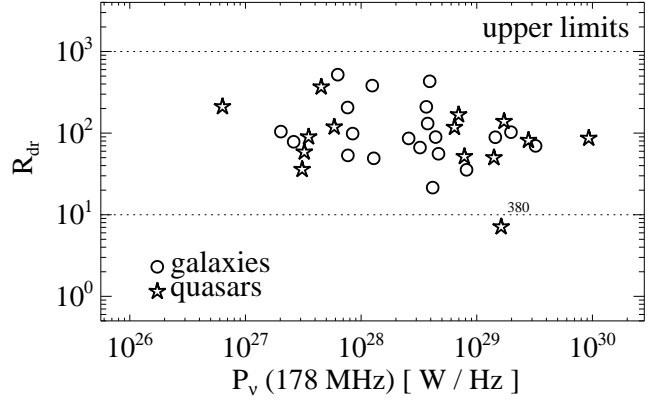


Fig. 7. Same as Fig. 6, but for the sources from Fig. 3 with IR upper limits only.

ing similarity of the R_{dr} distributions for *quasars* and *galaxies* provides strong evidence in favour of the basic role of the orientation-dependent *unification*.

4.2.3. Other influences

When looking at the radio maps, it becomes clear that the jet and lobe phenomena are of course also influenced by the circumgalactic environment and by evolution. Therefore it appears not appropriate, to consider and apply the three “principles” *unification*, *environment* and *evolution* on an exclusive either-or basis, rather the interplay of all three principles will help to understand the commonalities and differences of *galaxies* and *quasars*. The task now is to find strategies for disentangling the effects of the three principles. Firstly, we discuss our data in view of the receding torus model – this topic may be considered as *evolution* of the torus with luminosity.

4.2.3.1 Receding torus model

In this modification of the general orientation-unifying model (Lawrence 1991, Hill et al. 1996, review by Simpson 2003 and references therein) both the *galaxies* and the *quasars* are basically surrounded by a dusty torus, but the inner wall of the torus recedes with increasing luminosity of the central engine due to dust sublimation ($r_{sub} \propto L^{0.5}$, e.g. Netzer & Laor 1993). Under the assumption, that the scale height of the dust torus is independent of luminosity, the opening angle of the bi-cone increases with luminosity.

When defining those objects with direct view to the broad emission line region simply as *quasars* and all others as *galaxies*, then the receding torus model predicts that the *quasar* fraction increases with luminosity. In fact, such a transition of the *quasar* fraction from about 20% to higher values is observed at a 151 MHz luminosity threshold of about $10^{26.5}$ W/Hz (Willott et al. 2000). However, in all the luminosity bins above $10^{26.5}$ W/Hz the *quasar* fraction is 40% at the $1-\sigma$ level (Willott et al. 2000). This constancy of the *quasar* fraction at high luminosities is surprising in the frame of a pure receding torus model. It

suggests that above a luminosity threshold – possibly around $10^{26.5}$ W/Hz – the geometry of the receding torus does not change significantly and that the bi-cone opening angle has reached a maximum value compatible with other constraints. All of our FR 2 sources have 178 MHz luminosities higher than $10^{26.5}$ W/Hz (Fig. 6), hence lie above this threshold. With regard to our 3CR data we emphasize two points:

1) If *galaxies* and *quasars* belong to the same parent population, then – irrespective of whether a change of the source geometry with luminosity occurs or not – any orientation-dependent *unification* predicts that for a given luminosity bin the dust-to-lobe luminosity ratio R_{dr} should be the same for the *galaxy* and the *quasar*. If the *galaxy* had a lower R_{dr} than the *quasar*, this would point to a weaker central engine in the *galaxy*. In such a case, however, we cannot determine from the current data, whether this difference between *galaxy* and *quasar* is accompanied by different torus properties – and even if we could, this information would be only of moderate relevance with regard to other effects like lobe evolution and circumgalactic environment discussed in the next subsection. Nevertheless, our 3CR data show a striking similarity of the R_{dr} distributions for the *quasars* and the *galaxies* (Fig. 6) and any difference or decline with luminosity can be established at most at the $1-\sigma$ level or less (Table 3).

2) If the bi-cone opening angle increases significantly with luminosity, then the covering angle of the dust, which absorbs the radiation from the central engine, decreases. Then one would expect that – relative to another measure of the AGN strength – the IR luminosity declines. For example an increase of the half-opening angle of the bi-cone from 30° to $60-65^\circ$ results in a decrease of the dusty solid angle seen from the central source by a factor of about two ($\cos 30^\circ / \cos 65^\circ = 2.05$). We searched for such a relative decline of the IR luminosity in two data samples:

- a) If in *optically selected quasars* the blue continuum from the central engine is seen largely free of extinction, then the ratio of blue to IR luminosity should decline. We examined the sample of 64 Palomar Green quasars with good near- and mid-IR data and covering four decades in luminosity (Fig. 4 and Table 2 in Haas et al. 2003). We find that for all bins above $L_B = 10^{11} L_\odot$ (corresponding to $M_B < -24$ mag) the mean ratios of L_{NIR}/L_B and L_{MIR}/L_B are clearly constant at the $1-\sigma$ level with values about 1.1 ± 0.5 . But for the low luminosity bins with $L_B < 10^{11} L_\odot$ the ratios are higher by a factor of about 1.5 and 1.7, respectively, although the differences are only marginally significant.
- b) For the *radio-loud 3CR objects* one may expect a decline of R_{dr} with luminosity, but our data do not show a clear trend at a statistically significant level (Fig. 6, Table 3).

Thus we conclude that the effects of the receding torus with increasing bi-cone opening angle may be significant at lower luminosity levels for Seyfert galaxies and radio galaxies having 178 MHz luminosities below $10^{26.5}$ W/Hz, but that at the high luminosity level of quasars the receding torus model in its originally proposed rigid form plays only a minor role and needs some further refinement.

One refinement should focus on the torus scale height: For the receding torus model the assumption of a constant torus scale height is most critical. It may not be justified if the AGN phenomenon is accompanied by nuclear starbursts and if the star formation rate (SFR) grows with AGN luminosity. Then supernovae will blow-up the scale height h of the torus (and the disk) by injection of kinetic energy. For example, three-dimensional numerical simulations of the interstellar matter located in the combined gravitational potential of both a central black hole and a stellar system yield $h \propto \text{SFR}^{0.5} \propto L^{0.5}$ (Wada & Norman 2002). If this is the case, then both h and r_{sub} scale with $L^{0.5}$ and the opening angle of the bi-cone does not change with luminosity. This refinement would explain (1) that the quasar fraction remains constant at 151 MHz luminosities above $10^{26.5}$ W/Hz, and (2) that the ratios L_{NIR}/L_B and L_{MIR}/L_B do not decline at luminosities above $L_B = 10^{11} L_\odot$ ($M_B < -24$ mag).

4.2.3.2 Environment and lobe evolution

The ISO data suggest, that the FIR and MIR luminosities actually yield good estimates for the strength of the AGN. Now, under the premise that the *unification* is basically valid, sensitive infrared measurements offer to pursue the following strategy proposed by Barthel & Arnaud (1996): We adopt the IR luminosity as primary measure for the AGN power and examine the strength of the radio lobes. Then deviations in the dust-to-lobe luminosity ratio allow, free of orientation bias, to explore the additional influence of environment and evolution onto the extended radio lobes. In the following, we consider the extreme cases of high and low R_{dr} values in Fig. 6.

High values of R_{dr} are expected for sources, which are either rather dust-rich or do not show strong radio lobe activity. Examples are the “cool” FR 2 galaxies 3C 321 and 3C 459 both with a high FIR contribution possibly enhanced by starbursts. Very extreme examples for high R_{dr} sources are radio-quiet quasars lying even above the upper plot range of Fig. 6.

Low values of R_{dr} are expected for sources, which are either rather dust-poor or do show exceptional radio lobe activity – possibly caused by a special circumgalactic environment or by a high evolutionary state of the lobes. For example, 3C 405 (Cygnus A) has exceptionally bright radio lobes (Barthel & Arnaud, 1996) and shows a low $R_{\text{dr}} < 10$, confirming the suggestion by Barthel & Arnaud, that radio luminosity is not generally a good measure of AGN power. The ISO data show that the dust emission may serve as a better isotropic indicator for the AGN strength. Also the galaxy 3C 295 lies at the low end of the FIR-to-radio distribution, indicating high efficiency in creating the radio lobe luminosity. Note that 3C 295 is located in a dense X-ray bright cluster, suggesting the influence of the environment in enhancing the lobe power. Also 3C 380 is peculiar in that it shows both a relatively flat radio spectrum probably seen pole-on and bright FR 2 lobes. A possible way out of this dilemma is that there is an intrinsic bend in the jet (Wilkinson et al. 1991). In this case a strong interaction with the circumgalactic medium may provide an extraordinarily high radio luminosity, too.

The extreme cases with high and low R_{dr} show that the dispersion of the R_{dr} distribution in general may be well understood in terms of evolution of the radio lobes and by effects of the circumgalactic environment.

If evolutionary and environmental effects are superposed on the pure orientation-dependent unification, then it is a priori not clear whether the increased dispersion affects *galaxies* and *quasars* in the same manner, or whether a bias is introduced. A detailed investigation of the possible selection effects (Chapter 3.5.3 in Haas 2001) shows that there is a bias, which limits the strategies to check the *unification*: a radio source, which has already been recognised as a *quasar* due to some criteria, will on average always exhibit a higher IR luminosity than a source with matching radio luminosity, which has not yet been identified as a *quasar*. Larger data samples are required in order to overcome this "strategical bias".

5. Conclusions

We have obtained sensitive Infrared SEDs for a large sample of 3CR radio galaxies and quasars. In order to check the orientation-dependent *unification* of powerful FR 2 sources we considered 17 *galaxies* and 18 *quasars* with good IR detections. The main conclusions for this sample are:

- 1) Both the *quasars* and the *galaxies* exhibit a high mid- to far-IR luminosity ratio typical for AGNs.
- 2) The ratio of IR dust to radio lobe luminosity R_{dr} is similar for the *quasars* and the *galaxies*. Therefore, this result provides strong evidence in favour of the orientation-dependent *unification* of luminous ($L_{\text{IR}} \gtrsim 10^{11} L_{\odot}$) narrow line FR 2 radio *galaxies* with *quasars*.
- 3) The dispersion of the R_{dr} distribution might be caused by evolution by the radio lobes as well as effects of the circumgalactic environment.
- 4) The receding torus model in its original formulation is not valid at the high luminosity of our sources ($L_{\text{IR}} \gtrsim 10^{11} L_{\odot}$). Therefore we propose as a refinement that the scale height of the torus increases also with luminosity due to supernovae from starbursts accompanying the AGN.

Compared with the detections, the upper limits of the remaining 20 *galaxies* and 15 *quasars* are so high that they do not provide any deep constraints or conflicts with the conclusions above.

Acknowledgements. We thank the anonymous referee for constructive suggestions and for encouraging us to discuss the receding torus model. The ISOPHOT Data Centre at MPIA is supported by Deutsches Zentrum für Luft- und Raumfahrt e.V. (DLR) with funds of Bundesministerium für Bildung und Forschung, grant no. 50 QI 0201. IRAM is supported by INSU/CNRS (France), MPG (Germany) and IGN (Spain). Martin Haas thanks for grants from the Nordrhein-Westfälische Akademie der Wissenschaften, funded by the Federal State Nordrhein-Westfalen and the Federal Republic of Germany. This research is essentially based on data from the ISO and JCMT/SCUBA Archives. For literature and photometry search NED and SIMBAD were used. It is a pleasure to thank IRAM for discretionary observing time with the 30 m telescope at Pico Veleta.

Table 3. Average values of $\log(R_{\text{dr}})$ for galaxies and quasars shown in Figs. 6 and 7. The means \pm standard deviations are given for two bins in luminosity of L_{IR} and $P_{178\text{MHz}}$. N denotes the number of sources in the bins. The averages are also calculated excluding extreme outliers.

bins	quasars	N	galaxies	N
Detections:				
L_{IR}				
$< 2 \cdot 10^{12} L_{\odot}$	1.946 ± 0.290	6	1.907 ± 0.620	11
			1.900 ± 0.375	9 ^a
$> 2 \cdot 10^{12} L_{\odot}$	1.818 ± 0.327	12	1.859 ± 0.650	6
			1.640 ± 0.408	5 ^b
Detections:				
$P_{178\text{MHz}}$				
$< 2 \cdot 10^{28} \text{ W/Hz}$	1.970 ± 0.301	8	2.174 ± 0.548	10
			1.960 ± 0.351	8 ^c
$> 2 \cdot 10^{28} \text{ W/Hz}$	1.774 ± 0.308	10	1.484 ± 0.466	7
			1.603 ± 0.376	6 ^d
Upper limits:				
$P_{178\text{MHz}}$				
$< 2 \cdot 10^{28} \text{ W/Hz}$	2.197 ± 0.533	7	2.117 ± 0.382	8
	2.040 ± 0.367	6 ^e		
$> 2 \cdot 10^{28} \text{ W/Hz}$	1.819 ± 0.434	8	1.935 ± 0.337	12
	1.957 ± 0.203	7 ^f		

^a excluding the extremes 3C 321 and 3C405

^b excluding the extreme 3C 459

^c excluding the extremes 3C 321 and 3C459

^d excluding the extreme 3C 405

^e excluding the extreme 3C 371 (BL Lac type, outside Figure ranges)

^f excluding the extreme 3C 380

References

- Akujor C.E., Lüdke E., Browne I.W.A., et al., 1994, A&AS 105, 247
 Andreani P., Fosbury R.A.E., van Bemmell I., Freudling W., 2002 A&A 381, 389
 Antonucci R.R.J., 1984, ApJ 278, 499
 Antonucci R.R.J., Barvainis R., 1990, ApJL 363, L17
 Antonucci R.R.J., Miller J.S., 1985, ApJ 297, 621
 Archibald E.N., Dunlop J.S., Hughes D.H., et al., 2001, MNRAS 323, 417
 Barthel P.D., 1989, ApJ 336, 606
 Barthel P.D., Arnaud K.A., 1996, MNRAS 283, L45
 Barthel P.D., Miley G.K., 1988, Nature 333, 319
 Begelman M.C., Blandford R.D., Rees M. J., 1984, RvMP 56, 255
 Bennett C.L., Halpern M., Hinshaw G., et al. 2003, ApJS, 148, 1
 Best P.N., Röttgering H.J.A., Bremer M.N., et al., 1998, MNRAS 301, L15
 Blundell K., Rawlings S., 1999, Nature 399, 330
 Cesarsky C., Abergel A., Agnese P., et al., 1996, A&A 315, L32
 Chiaberge M., Capetti A., Celotti A., 1999, A&A 349, 77
 Chiaberge M., Capetti A., Celotti A., 2000, A&A 355, 873
 Chini R., Kreysa E., Biermann P.L., 1989a, A&A 219, 87
 Chini R., Biermann P.L., Kreysa E., Gmünd H.-P., 1989b, A&A 221, L3
 Cohen M.H., Ogle P.M., Tran H.D., Goodrich R.W., Miller J.S., 1999, AJ 118, 1963
 de Vaucouleurs G., de Vaucouleurs A., Corwin jr. H.G., et al. 1991, 'Third reference catalog of bright galaxies', Version 3.9, Springer-Verlag, Berlin

Table 1. Measured flux densities in mJy as a function of wavelength in μm . Numbers in bold are detections above the $3\text{-}\sigma$ level, the uncertainties are 10–30%. Other numbers represent $3\text{-}\sigma$ upper limits. The apertures used for each filter are listed underneath the wavelength; for 120–200 μm the apertures were 90'' in the case of maps and 180'' in the case of chopped photometry. "m" and "c" denote mapped/chopped observations. The previous publications of ISOPHOT flux values refer to: A = Andreani et al. (2002), vB = van Bemmelen et al. (2000), F = Fanti et al. (2000), H1 = Haas et al. (1998), H2 = Haas et al. (2003), M = Meisenheimer et al. (2001), P = Polletta et al. (2000). In addition to our photometry, we list also the SCUBA $F_{450\mu\text{m}}$ and $F_{850\mu\text{m}}$ literature values shown in the SED plots: They are taken from A = Archibald et al. (2001), B = Best et al. (1998), H = Hughes et al. (1993, at 800 μm), P = Polletta et al. (2000), R = Robson et al. (1998), vB = van Bemmelen et al. (2000), W = Willott et al. (2002).

3C	publ	map/ chop	4.8 23''	7.3 23''	10 23''	11.5 23''	12.8 23''	16 23''	20 52''	25 52''	map/ chop	60 45''	80 45''	90 45''	100 45''	map/ chop	120	150	170	180	200	450 8''	850 15''	1200 11''
2.0*		c								<21	m	72		158		m			<609					
9.0	M	c	3				<42		50		c	<144		<246		c			<327			<11.4		
16.0	F	c									c	<129		<162		c			<177		<450		<3.3	
17.0*		m				<48										m			<33			290.0		
19.0	vB,F										m	<60		<42		m			<117		<495			
20.0	H1,M	m								<33	c	97		223		m			167				<5.7	
33.0											m		161									9.5		
33.1		m				14			26		m	48		41		m			<66				5.8	
34.0	F										m	<48		<60		m			<189		<426		<6.0	
42.0	vB,F										m	<78		<45		m			<417		<360		5.2	
46.0	A,F										c	<48		<75		c			<264		<900			
47.0	M,P	m	<9			10				43	c	103		159		m			164				10.8	
48.0	H1,M	c	20			50			108		c	460		829		m	730		554	420		<63	7.2	
49.0											c	120		<162		c			<585		<675			
61.1		m				<3				<15	m	33		44		m			<60				3.0	
65.0	M	m	2			8				26	c	129		<129		m			<99				<11.4 ^H	
67.0	vB,F	c				<15					m	<78		<60		m			<444					
68.1		c						<39	<57	<54						c							<6.3	
79.0	F										c	144		116		c			<585		<900		<2.1	
84.0											m					m			4153		1956			
109.0		m		31		58				170	m	203		158		m		<582			<813			39.0
138.0	M	m				11				24	m	<48		<105		m			<117				107	
234.0		c	16	41		100				276	c	315		261		c		<162		<1125				4.1
245.0											c	196		<153		c			<558					
249.1		c	9	14		18				40	m	60		40		m		<90		<90			<7.2 ^P	
268.3	A,F	c				<24					c	<69		<84		c			<720		<750			
268.4	A										c			54^c		c			586^c			<37.5 ^W	5.1 ^W	
270.0*											c	<291		492		c			661		<900		200	210
272.1											c	700		1000		c			703		<900			137.0
273.0	M										c	1124	1291		1348		c	1546	1113	1292	1056	1091		
274.0											c	610		954		c			322		<516		1320	2480
274.1	F										c	<222		<432		c			<702		<675			<5.1
277.1*	vB										m	<144		<90		m			<93					
277.2	F										m	146		92		m			<156				<32 ^A	<3.0 ^A
280.0	A,M	c	<3	<12			<66		<96		c	145		<126	<189	c			<231					
280.1											c			<75		c							<71.4 ^W	<5.2 ^W
284.0*	F										c		157	<285		c			<135		<567			
286.0	A,M	c	<9				<93		<117		c	131		105		c			<186				259	
287.0	A,M	c	<18				<69		<126		c	<156		<78		c							85	
288.1*	A	c								<18	c	<75		127		c			<105					<4.2
289.0											m			<39		m			<48					
293.0																							<4.2	
295.0	A,F,M	c	3	<12			<30		<48		c	87		<291		c			<111					
298.0*	M	c	<12				23		29		c	184		213		c			243				<71 ^W	21.1 ^W
299.0	F															c				<450				
303.1	F										c	<111		74		c			<480		<390			
309.1	A,F										c	118		<144		c			<273				<26	
318.0	F										c	157		284		c			391		<657		<32 ^W	7.8 ^W
321.0											c			780		m			402				<20	
323.1*	vB,H2	c	11	16		25				43	m	45		33		m			<57				<9.0 ^{vB}	
324.0	M										c	<102		<231		c			<237				<21 ^B	3.0 ^B
325.0	A,M	c	<39	<18			<75		<81		c	160		140		c			<126				<25	
330.0	F										m	<75		<45		m			<123		<540			<3.2
332.0*		m								<150	m	<216		<132		m			<225					<10.2
334.0	vB										m	86		56		m			<60				<14	8.3

* contained in Spinrad et al. (1985), but not in Laing et al. (1983); ^c contaminated by NGC 4138; ^x possibly contaminated by an asteroid;

^s integrated over spectral continuum obtained with ISOPHOT-S; ⁺ also: 1060 mJy at 65 μm

Table 1. continued.

3C	publ	map/ chop	4.8 23"	7.3 23"	10 23"	11.5 23"	12.8 23"	16 23"	20 52"	25 52"	map/ chop	60 45"	80 45"	90 45"	100 45"	map/ chop	120	150	170	180	200	450 8"	850 15"	1200 11"
336.0	A,F	c	<15	<6	<12			<36	<75	<42	c	<96		<168		c		<468				<47	<5.5	
337.0		m									m	<63		<78		m		<102						
340.0		m									m			<99		m		<168				<27 ^A	<2.6 ^A	
343.1	A,F	c									c	<108		<462		c		<411						7.6
351.0	vB,H2	c	18	31	50					112	m	201	168	151		m	94	66		48				<3.3
352.0	A										m			<75		m		<156						
356.0	A										m			27		m		<84				<60 ^A	<3.1 ^A	
368.0	M	c	4 ^x	16 ^x			<120		<162		c	94		<144		c		<168				<45 ^A	4.1 ^A	
371.0*											c			397		c		275						
var.											c			226		c		215						
380.0	M	c	<9	7	<18					<66	m	54		56		m		83					659	
381.0		m			19					52	m	74		<78		m		42						<2.1
390.3		c		55 ^s						139	c	191		<1233		c	<963		<984			<385	<14	
401.0	F										c	<78		<99		c		<351		<270			12.2	
405.0*	H1,M,P	c	<12	40			250		590		c	3034		2155		m	994		419			~230 ^R	~490 ^R	628
427.1	M	c	<48	<15			<114		<75		c	<135		<204		c		<180						
437.0	M	c	<21	<12			<102		<138		c	<126		<246		c		<189				<52 ^W	<3.0 ^W	
441.0	F										c	<174		<153		c		<234		<324				<3.0
445.0*		c	46	73						360	c	435		<357		c		<849		<1647				<4.8
454.3		c	<12	16			34		<291		c	706		324		m	187		248			1370	2780	3716.0
459.0*	F								<450		c	1035 ⁺		1375		c		1110	815	<1413				
460.0	vB	m									m	<57		<54		m		<351						

Fanti C., Pozzi F., Fanti R., et al., 2000, A&A 358, 499
 Freudling W., Siebenmorgen R., Haas M., 2003, ApJL 599, L13
 Haas M., 2001, Habilitationsschrift Universität Heidelberg, available from <http://www.astro.ruhr-uni-bochum.de/haas/>
 Haas M., Chini R., Meisenheimer K., et al., 1998, ApJL 503, L109
 Haas M., Müller S.A.H., Chini R., et al., 2000, A&A 354, 453
 Haas M., Klaas U., Müller S.A.H., Chini R., Coulson I., 2001, A&A 367, L9
 Haas M., Klaas U., Müller S.A.H., et al., 2003, A&A 402, 87
 Heckman T.M., Chambers K.C., Postman M., 1992, ApJ 391, 39
 Heckman T.M., O'Dea Ch.P., Baum S.A., Laurikainen E., 1994, ApJ 428, 65
 Hes R., Barthel P.D., Hoekstra H., 1995, A&A 303, 8
 Hildebrand R.H. 1983, QJRAS 24, 267
 Hill G.J., Goodrich R.W., Depoy D.L., 1996, ApJ 462, 163
 Hine R.G., Longair M.S., 1979, MNRAS 188, 111
 Hoekstra H., Barthel P.D., Hes R., 1997, A&A 319, 757
 Hughes D.H., Robson E.I., Dunlop J.S., Gear W.K., 1993, MNRAS 263, 607
 Kaiser C.R., Dennett-Thorpe J., Alexander P., 1997, MNRAS 292, 723
 Kellermann K.I., Sramek R., Schmidt M., et al., 1989, AJ 98, 1195
 Kessler M.F., Steinz J.A., Anderegg M.E., et al., 1996, A&A 315, L27
 Kessler M.F., Müller T.G., Arviset C., García-Lario P., & Prusti T. 2000, *The ISO Handbook*, SAI/2000-035/Dc, ESA publ.
 Klaas U., Laureijs R., Radovich M., Schulz B., Wilke K., 2002, "ISOPHOT calibration accuracies, V5.0 (adapted to OLP10)" ISO Explanatory Library Doc. SAI/02-xxx/rp, ESA publ.
 Klaas U., Haas M., Müller S.A.H., et al., 2001, A&A 379, 823
 Kreysa E., Gemünd H.-P., Gromke J., et al., 1998, SPIE 3357, 319
 Kühr H., Witzel A., Pauliny-Toth I.I.K., Nauber U., 1981, A&AS 45, 367
 Laing R.A., Riley J.M., Longair M.S., 1983, MNRAS 204, 151
 Laureijs R., Klaas U. 1999, ISOPHOT Error Budgets V1.0, ISO Explanatory Library Doc. SAI/98-091/dc, ESA publ.

Laureijs R., Klaas U., Richards P.J., Schulz B., Abraham P., 2002, *The ISO Handbook*, Vol. IV: PHT – the Imaging Photo-Polarimeter, Version 2.0, SAI/99-069/dc, ESA publications
 Lawrence A., 1991, MNRAS 252, 586
 Lemke D., Klaas U., Abolins J., et al., 1996, A&A 315, L64
 Lilly S.J., Longair M.S., 1984, MNRAS 211, 833
 Lilly S.J., Longair M.S., Miller L., 1985, MNRAS 214, 109
 Meisenheimer K., Haas M., Müller S.A.H., et al., 2001, A&A 372, 719
 Miley G., Neugebauer G., Soifer B.T., et al., 1984, ApJL 278, L79
 Neugebauer G., Green R.F., Matthews K., et al., 1987 ApJS 63, 615
 Netzer H., Laor A., 1993, ApJL 404, L51
 Orr M.J.L., Browne I.W.A., 1982, MNRAS 200, 1067
 Pier E.A., Krolik J.H., 1992, ApJ 401, 99
 Pier E.A., Krolik J.H., 1993, ApJ 418, 673
 Polletta M., Courvoisier Th., Hooper E.J., Wilkes B.J., 2000, A&A 362, 75
 Robson E.I., Leeuw L.L. Stevens J.A., Holland W.S., 1998, MNRAS 301, 935
 Saunders R., Baldwin J.E., Rawlings S., Warner P.J., Miller L., 1989, MNRAS 238, 777
 Simpson C., 2003, New Astron. Rev. 47, 211
 Simpson C., Ward M., Wall J.V., 2000, MNRAS 319, 963
 Singal, A.K., 1996, MNRAS 278, 1069
 Siebenmorgen R., Freudling W., Krügel E., Haas M., 2004, A&A in press, astro-ph/0404040
 Spinrad H., Djorgowski S., Marr J., Aguilar L., 1985, PASP 97, 932
 Steppe H., Salter C.J., Chini R., et al., 1988, A&AS 75, 317
 Steppe H., Liechti S., Mauersberger R., et al., 1992, A&AS 96, 441
 Steppe H., Paubert G., Sievers A., et al., 1993, A&AS 102, 611
 Stevens J. A., Robson E. I., Gear W. K., et al., 1998, ApJ 502,
 Stickel M., Lemke D., Klaas U., et al., 2000, A&A 359, 865
 Urry C.M., Padovani P., 1995, PASP 107, 803
 van Bemmell I.M., Barthel P., de Graauw Th., 2000, A&A 359, 523
 van Bemmell I.M., Bertoldi F., 2001, A&A 368, 414
 van Bemmell I.M., Dullemond C.P., 2003, A&A 404, 1

Table 2. Types, redshifts and luminosity distances, restframe luminosities, dust temperatures and masses. The luminosity distance D_L is calculated adopting a Λ cosmology with $H_0 = 71 \text{ km s}^{-1} \text{ Mpc}^{-1}$, $\Omega_{\text{matter}} = 0.27$ and $\Omega_{\Lambda} = 0.73$. The luminosities L_{opt} ($0.5\text{-}1 \mu\text{m}$), L_{NIR} ($3\text{-}10 \mu\text{m}$), L_{MIR} ($10\text{-}40 \mu\text{m}$) and L_{FIR} ($40\text{-}1000 \mu\text{m}$) are computed in the restframes of the objects from the “envelopes” of the SEDs. The luminosities give the total emission from host galaxy and the core. The IR luminosities largely represent the thermal dust luminosities, except for some sources (like 3C 371 or 3C 380), which do not exhibit any prominent thermal bump and are excluded from the discussion. The thermal dust emission power νP_{ν} has been computed at restframe wavelengths 15 and 70 μm , respectively. The 178 MHz radio lobe power is computed from the observed 178 MHz fluxes, applying a K-correction with a spectral index $\alpha = 0.5$. The choice of α has only little impact on the resulting lobe power and the relations discussed. R_{dr} is the ratio of dust power to radio lobe power at 15 and 70 μm , respectively. The values of T_p refer to the peak blackbody shown in the SED plots, the uncertainty is 5-10 K and can raise to 50% in cases of poor FIR upper limits. The dust mass M_{dust} is estimated according to Formula 6 in Stickel et al. (2000) following Hildebrand (1983), with uncertainties up to an order of magnitude. A “ \sim ” marks highly uncertain $L_{\text{MIR}}/L_{\text{FIR}}$, T_{dust} and M_{dust} values due to poor dust bump determinations or upper limit constraints, and these sources are not used in the discussion.

3CR	type*	redshift	D_L Mpc	L_{opt} log [L_{\odot}]	L_{NIR} log [L_{\odot}]	L_{MIR} log [L_{\odot}]	L_{FIR} log [L_{\odot}]	$L_{\text{MIR}}/L_{\text{FIR}}$	P(15 μm) log [W]	P(70 μm) log [W]	P(178 MHz) log [W]	R_{dr} 15 μm	R_{dr} 70 μm	T_p [K]	M_d log [M_{\odot}]
2.0	QSR C CSS	1.037	6943	11.39	<12.00	12.80	12.61	1.54	39.11	39.09	37.34	59	57	55	7.92
9.0	QSR L	2.012	15852	12.76	13.85	<13.87	<13.62	~ 1.79	<40.28	<40.16	38.22	< 115	< 87	~ 50	~ 8.99
16.0	LERG FR 2	0.405	2193	10.38	<11.31	<11.85	<11.90	~ 0.89	<38.11	<38.45	36.13	< 95	< 206	~ 40	~ 7.81
17.0	BLRG ?	0.220	1081	10.37	10.67	<10.65	<10.96	~ 0.49	<37.06	<37.54	35.74	< 21	< 63	~ 40	~ 6.91
19.0	NLRG FR 2	0.482	2701	10.80	<11.29	<11.50	<11.47	~ 1.06	<37.87	<38.05	36.36	< 32	< 49	~ 40	~ 7.41
20.0	NLRG FR 2	0.174	830	9.93	10.52	10.95	11.18	0.58	37.21	37.68	35.83	24	70	35	7.45
33.0	NLRG FR 2	0.059	261	10.31	9.93	<10.06	10.14	0.83	<36.45	36.72	34.92	< 34	63	35	6.40
33.1	BLRG FR 2	0.181	869	10.15	10.96	11.00	10.61	2.47	37.47	37.14	35.36	129	60	50	6.08
34.0	NLRG FR 2	0.689	4177	11.01	<11.70	<12.09	<12.03	~ 1.16	<38.41	<38.58	36.76	< 45	< 67	~ 40	~ 7.95
42.0	NLRG FR 2	0.395	2128	10.60	<10.69	<11.12	<11.28	~ 0.70	<37.42	<37.86	36.14	< 19	< 53	~ 40	~ 7.23
46.0	NLRG FR 2	0.437	2400	10.91	<11.37	<11.63	<11.61	~ 1.06	<37.98	<38.17	36.18	< 64	< 99	~ 40	~ 7.54
47.0	QSR L	0.425	2322	11.09	11.62	12.01	11.91	1.24	38.38	38.48	36.56	65	84	35	8.18
48.0	QSR C CSS	0.367	1950	11.64	12.21	12.44	12.47	0.93	38.79	39.02	36.72	117	203	35	8.70
49.0	NLRG FR 2 CSS	0.621	3675	10.48	<11.65	12.28	12.34	0.88	38.52	38.90	36.58	87	209	40	8.26
61.1	NLRG FR 2	0.186	895	9.89	10.02	10.28	10.59	0.49	36.47	37.16	35.76	5	25	40	6.54
65.0	NLRG FR 2	1.176	8125	11.11	12.71	13.10	12.51	3.94	39.42	38.95	37.50	83	29	80	7.17
67.0	BLRG FR 2 CSS	0.310	1600	10.50	<10.96	<11.17	<11.17	~ 1.01	<37.54	<37.75	35.80	< 55	< 90	~ 40	~ 7.11
68.1	QSR L	1.238	8664	12.13	<12.31	<12.65	<13.06	~ 0.39	<38.96	<39.63	37.49	< 30	< 139	~ 40	~ 8.01
79.0	NLRG FR 2	0.256	1283	10.66	11.08	11.58	11.38	1.60	37.94	37.94	36.08	73	73	55	6.63
84.0	NLRG FR 1	0.018	74	10.61	10.46	10.87	10.80	1.18	37.11	37.30	33.85	1831	2779	35	7.01
109.0	BLRG FR 2	0.306	1577	11.28	12.06	12.22	11.69	3.38	38.67	38.21	36.12	362	126	55	6.95
138.0	QSR C CSS	0.759	4707	11.45	12.24	12.38	<12.29	~ 1.23	38.81	<38.86	37.14	47	< 52	~ 40	~ 8.20
234.0	NLRG FR 2	0.185	890	10.56	11.64	11.95	11.50	2.81	38.39	38.04	35.76	426	189	45	7.17
245.0	QSR L	1.029	6876	11.83	12.49	13.09	12.60	3.03	39.38	38.94	37.32	115	42	85	7.08
249.1	QSR L	0.311	1607	11.60	11.70	11.66	11.16	3.14	38.11	37.57	35.83	191	55	60	6.26
268.3	BLRG FR 2 CSS	0.371	1975	10.27	<11.22	<11.57	<11.54	~ 1.08	<37.90	<38.09	36.02	< 77	< 119	~ 40	~ 7.46
270.0	NLRG FR 1	0.007	31	10.28	9.50	8.84	9.05	0.61	35.10	35.51	33.03	< 120	305	28	5.81
272.1	LERG FR 1	0.003	12	10.25	9.43	8.13	8.33	0.63	34.46	34.77	31.90	361	736	27	5.13
273.0	QSR FR 2	0.158	747	12.13	12.28	12.13	12.00	1.35	38.56	38.47	35.91	453	368	30	8.53
274.0	NLRG FR 1	0.004	16	10.29	9.56	8.43	8.50	0.86	34.72	35.01	32.56	144	286	35	4.75
274.1	NELR FR 2	0.422	2303	10.67	<11.56	<12.12	<12.34	~ 0.60	<38.38	<38.93	36.35	< 108	< 382	~ 40	~ 8.30
277.1	QSR FR 2	0.321	1667	10.90	<11.23	<11.60	<11.16	~ 2.78	<37.93	<37.59	35.76	< 147	< 67	~ 40	~ 6.95
277.2	NLRG FR 2	0.766	4761	10.89	<11.86	12.71	12.13	3.82	38.89	38.51	36.89	101	42	90	6.58
280.0	NLRG FR 2	0.996	6602	10.98	<12.23	12.97	12.36	4.02	39.19	38.73	37.49	49	17	90	6.81
280.1	QSR FR 2	1.659	12481	11.95	<12.67	<13.03	<13.12	~ 0.82	<39.38	<39.61	37.70	< 48	< 82	~ 40	~ 8.28
284.0	NLRG FR 2	0.239	1187	10.82	<11.19	<11.49	11.55	0.89	<37.84	38.11	35.58	< 182	344	40	7.49
286.0	QSR C CSS	0.849	5410	11.94	12.01	12.66	12.28	2.42	38.87	38.71	37.33	35	24	75	7.00
287.0	QSR C CSS	1.055	7094	11.92	<12.18	<12.51	<12.54	~ 0.93	<38.84	<39.10	37.40	< 28	< 50	~ 40	~ 8.47
288.1	QSR L	0.961	6313	11.75	12.01	12.66	12.51	1.43	38.97	39.02	37.03	87	98	55	7.78
289.0	NLRG FR 2	0.967	6362	11.21	<11.82	<12.16	<12.15	~ 1.02	<38.49	<38.71	37.16	< 21	< 36	~ 40	~ 8.08
293.0	LERG FR 1	0.045	197	10.52	10.07	9.98	10.43	0.36	36.32	36.85	34.04	191	655	26	7.41
295.0	NLRG FR 2	0.461	2559	11.09	11.29	11.81	11.99	0.67	38.07	38.57	37.15	8	< 26	40	7.94
298.0	QSR FR 2	1.436	10427	12.77	13.32	13.52	13.19	2.17	39.88	39.70	38.24	44	29	40	9.06
299.0	NLRG FR 2 CSS	0.367	1950	10.48	<11.05	<11.68	<12.35	~ 0.21	<37.78	<38.94	36.05	< 53	< 780	~ 40	~ 8.30
303.1	NLRG FR 2 CSS	0.267	1347	10.61	10.56	10.83	11.11	0.52	37.10	37.71	35.55	36	145	40	7.07
309.1	QSR C CSS	0.905	5858	12.05	12.40	12.79	12.39	2.51	39.10	38.82	37.36	55	29	70	7.22
318.0	QSR FR 2 CSS	1.574	11690	11.62	<12.86	13.56	13.38	1.51	39.80	39.89	37.76	111	134	55	8.64
321.0	NLRG FR 2	0.096	435	10.60	10.60	11.33	11.36	0.92	37.45	37.86	34.76	497	1258	35	7.49
323.1	QSR FR 2	0.264	1329	11.42	11.62	11.53	10.88	4.49	38.03	37.38	35.61	261	59	60	5.98
324.0	NLRG FR 2	1.206	8385	11.25	12.12	<13.00	<13.01	~ 0.98	<39.16	<39.56	37.55	< 41	< 103	~ 50	~ 8.42

* The types are abbreviated as:

QSR = quasar, BLRG = broad line radio galaxy, NLRG = narrow line radio galaxy, LERG = low-excitation radio galaxy, C = core dominated, L = lobe dominated, FR 1, FR 2 = Fanaroff-Riley classes 1 and 2, CSS = compact steep spectrum source, OVV = optically violent variable.

Table 2. continued

3CR	type*	redshift	D _L Mpc	L _{opt} log [L _⊙]	L _{NIR} log [L _⊙]	L _{MIR} log [L _⊙]	L _{FIR} log [L _⊙]	L _{MIR} / L _{FIR}	P(15 μm) log [W]	P(70 μm) log [W]	P(178 MHz) log [W]	R _{dr} 15 μm	R _{dr} 70 μm	T _d [K]	M _d log M _⊙
325.0	QSR L	0.860	5498	11.43	<13.10	13.07	12.42	4.54	39.54	38.84	37.14	252	50	75	7.14
330.0	NLRG FR 2	0.550	3168	11.08	11.29	<11.54	<11.62	~ 0.83	<37.86	<38.20	36.87	< 10	< 21	~ 40	~ 7.57
332.0	BLRG FR 2	0.152	716	10.87	10.70	10.78	<10.80	~ 0.93	37.14	<37.38	35.05	122	< 211	~ 40	~ 6.75
334.0	QSR L	0.555	3203	11.54	<12.03	12.20	11.68	3.30	38.58	38.11	36.47	127	44	75	6.39
336.0	QSR L	0.927	6036	11.79	11.93	<12.64	<12.75	~ 0.77	<38.83	<39.32	37.09	< 55	< 168	~ 40	~ 8.69
337.0	NLRG FR 2	0.635	3777	10.66	<11.60	<12.08	<12.04	~ 1.09	<38.36	<38.60	36.66	< 50	< 86	~ 40	~ 7.96
340.0	NLRG FR 2	0.775	4830	10.77	<11.75	<12.22	<12.37	~ 0.70	<38.51	<38.94	36.83	< 48	< 131	~ 40	~ 8.32
343.1	NLRG FR 2 CSS	0.750	4638	11.13	<11.83	<12.46	<12.89	~ 0.37	<38.65	<39.48	36.84	< 64	< 431	~ 40	~ 8.85
351.0	QSR L	0.371	1975	11.80	12.22	12.27	11.87	2.50	38.68	38.39	36.13	360	185	50	7.30
352.0	NLRG FR 2	0.806	5071	10.57	<11.56	<12.10	<12.27	~ 0.68	<38.37	<38.84	36.92	< 28	< 84	~ 40	~ 8.22
356.0	NLRG FR 2	1.079	7296	11.23	11.52	12.02	12.25	0.59	38.28	38.83	37.27	10	37	40	8.20
368.0	NLRG FR 2	1.131	7738	11.35	<12.39	12.92	<12.82	~ 1.26	39.21	<39.36	37.41	63	< 89	~ 40	~ 8.73
371.0	BL Lac	0.051	224	10.77	<10.70	<10.63	<10.23	~ 2.49	<37.10	<36.73	33.59	<3227	<1373	~ 40	~ 6.11
380.0	QSR C CSS	0.692	4199	11.88	<12.28	<12.33	<11.85	~ 3.01	<38.76	<38.31	37.46	< 20	< 7	~ 65	~ 6.81
381.0*	NLRG FR 2	0.160	758	10.43	10.91	11.10	10.65	2.82	37.51	37.15	35.34	147	64	40	6.70
390.3	BLRG FR 2	0.056	246	10.30	10.64	10.65	10.23	2.61	37.13	36.76	34.80	211	90	40	6.13
401.0	LERG FR 2	0.201	976	10.72	<10.15	<10.51	<11.00	~ 0.33	<36.52	<37.56	35.67	< 7	< 78	~ 40	~ 6.94
405.0	NLRG FR 2	0.056	246	9.95	10.55	11.38	11.30	1.19	37.64	37.84	37.07	4	6	50	6.78
427.1	LERG FR 2	0.572	3324	10.59	<10.90	<11.99	<12.29	~ 0.50	<37.92	<38.85	36.89	< 11	< 89	~ 40	~ 8.21
437.0	NLRG FR 2	1.480	10827	11.15	<12.35	<13.33	<13.12	~ 1.63	<39.50	<39.60	37.76	< 55	< 70	~ 60	~ 8.21
441.0	NLRG FR 2	0.707	4311	10.72	<11.72	<12.26	<12.42	~ 0.68	<38.52	<38.99	36.81	< 51	< 150	~ 40	~ 8.36
445.0	BLRG FR 2	0.056	247	10.26	10.87	10.98	10.50	3.02	37.46	37.03	34.52	855	323	50	5.96
454.3	FSQ C OVV	0.860	5498	12.50	<12.92	13.53	12.79	5.59	39.81	39.13	37.06	566	118	100	7.10
459.0	NLRG FR 2	0.220	1081	10.89	11.07	11.83	12.24	0.39	37.93	38.81	35.85	120	908	40	8.18
460.0	NLRG FR 2	0.268	1353	10.39	<10.15	<10.43	<10.98	~ 0.28	<36.55	<37.58	35.56	< 10	< 104	~ 40	~ 6.94

* 3C381 could be classified as BLRG based on a noisy H_β line, which appears to be broader than the [OIII]λ5007 line, but with considerable uncertainty (Saunders et al. 1989). A new spectrum obtained at the KECK telescope shows that 3C381 should be classified as NLRG (van Bemmell, private communication).

Wada K., Norman C, 2002, ApJL 566, L21

Wilkinson P.N., Akujor C.E., Cornwell T.J., Saikia D.J., 1991, MNRAS 248, 86

Willott C.J., Rawlings S., Blundell K.M., Lacy M., 2000, MNRAS 316, 449

Willott C.J., Rawlings S., Archibald E.N., Dunlop J.S., 2002, MNRAS 331, 435

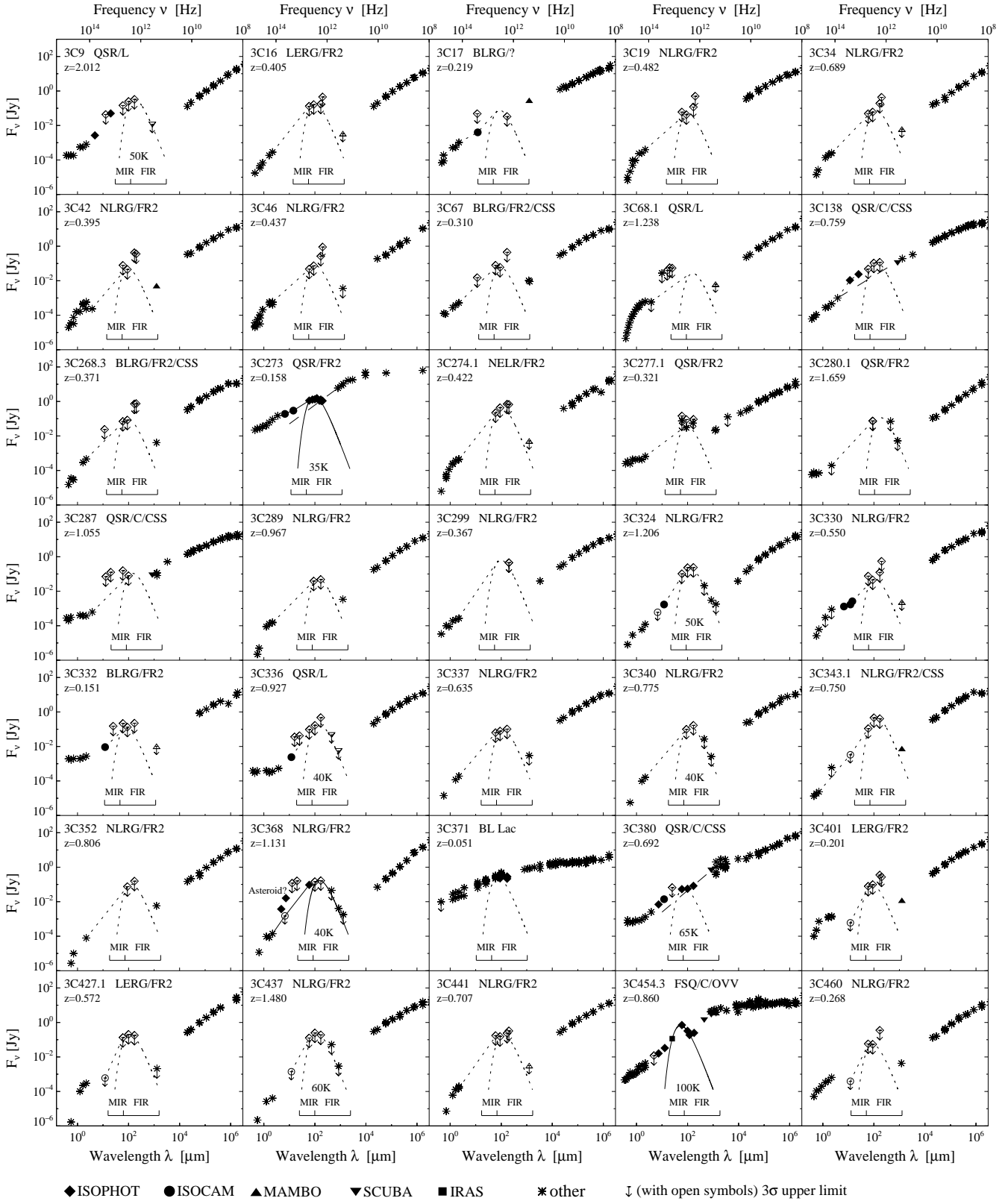


Fig. 3. Spectral energy distributions of the remaining sources not used in the discussion, which are either flat spectrum sources or have only poorly constrained thermal bumps. The meaning of the lines and labels is as in Fig. 1. For the poorly constrained cases, however, the blackbody curves and the envelopes are shown here as *dotted* lines in order to emphasize that they represent only a maximum possible dust contribution. For the blackbody, if not sufficiently constrained by the data, we adopted the average of $T_p \approx 40$ K derived from the good cases shown in Fig. 1. The long dashed lines for 3C 138, 3C 273 and 3C 380 indicate the extrapolation of the synchrotron emission towards shorter wavelengths.